Volume 1 | Number 1 | Jan 2013 | Pages 1–100

Journal of
Materials Chemistry B

Materials for biology and medicine
www.rsc.org/materialsB

ROYAL SOCIETY OF CHEMISTRY

ROYAL SOCIETY OF CHEMISTRY

www.rsc.org/materialsB

Journal of Materials Chemistry B

ARTICLE

Preventing high-temperature oxidation of Co−Cr-based dental alloys by boron doping

Kenta Yamanaka,[a,†] Manami Mori,[a,b] Kazuyo Ohmura,[a] and Akihiko Chiba[a]

Biomedical Co−Cr-based alloys used in dental restorations are usually subjected to high-temperature treatments during manufacturing. Therefore, it is practically essential to characterise and control the oxide films formed on the surfaces of these alloys during the heat treatment in terms of the materials loss, the accuracy of fit, and the aesthetics of the dental restorations. In this work, the effects of boron doping on the surface oxide films formed on Ni-free Co−28Cr−9W−1Si (mass%) dental alloys under short-term exposure to high temperatures, which simulate the manufacturing process of porcelain-fused-to-metal (PFM) restorations, were investigated. The surface oxides primarily consisted of Cr_2O_3 in all prepared alloys. The chemical composition of these surface layers varies with the B concentration in the bulk, with the addition of boron stabilising the dense Cr_2O_3 phase in the oxide films. Nanoscale boron enrichment is clearly observed at the interface between the oxide films and the metal substrate, with the oxidation of boron atoms leading to the formation of a B_2O_3 layer. Since B_2O_3 and Cr_2O_3 prevent oxygen diffusion, the surface oxide films on the boron-containing alloys are thinner; however, no additional thinning was observed when increasing the boron content from 0.01 to 0.8 mass%. It was also found that small amount of boron does not degrade the corrosion properties of the alloys in a 0.9% NaCl solution. The results obtained in this study will aid in the improvement of manufacturing processes, and ultimately, the performance of the PFM restorations.

Introduction

The excellent wear and corrosion resistance of Co−Cr-based alloys is exploited in a range of devices designed to operate under severe environmental conditions, from high-temperature structural superalloys to various biomedical applications such as orthopaedic and dental implants. Porcelain-fused-to-metal (PFM) restorations are widely used in dentistry because of their mechanical rigidity and pleasing aesthetics, which respectively stem from their metallic framework and the use of ceramic veneers.[1,2] The reliability of PFM restorations is well known, with remarkable survival rates having been reported.[3] For these applications, Ni-free Co−28Cr-based (mass%) alloys have replaced Au-based alloys as the material of choice owing to their lower cost (absence of precious elements) and better biocompatibility.[4,5]

The effects and mechanisms of oxidation in these alloys at high temperatures have been widely studied owing to its potential impact on their performance, notably at high temperatures. In addition, a better resistance to oxidation reduces the material loss during manufacturing. The bond strength between the metal frame and the porcelain veneer is another important aspect to be considered for PFM applications, as a pre-oxidation heat treatment is sometimes performed on dental alloys at temperatures as high as 1273 K to improve attachment.[6,7] However, whether oxidation during this treatment step affects the resulting bond strength is still a matter of debate. A few studies have reported that oxidation of the alloy surface lowers the strength of the bond between the metal substrate and the porcelain.[8–10] In contrast, Wu et al. found that the oxidation heat treatment had no significant effect on the porcelain bond strength for a selection of metal alloys.[11] The bond strength is, in any case, closely related to the surface state of the base metal; therefore, characterisation of the surface oxide film is crucial for optimising the alloy design and performance.

Furthermore, the uncovered portion of the metal framework using Co−Cr-based alloys is exposed to air during sintering (usually at ~1273 K) of the porcelain veneer,[8] leading to the formation of oxides which have to be descaled by shot blasting to ensure an aesthetically pleasing result. However, this results in material loss and reduces the fitting accuracy of the prosthesis. Therefore, further improvements in Co−Cr-based dental alloys are reliant on a better understanding of their oxidation at high temperatures.

Recently, we systematically investigated the effects of the alloying elements Si, C, and N, on the phase stability, microstructure, and mechanical properties of Co−28Cr−9W−

[a.] Institute for Materials Research, Tohoku University, 2-1-1 Katahira, Aoba-ku, Sendai 980-8577, Japan.
[b.] Department of Materials and Environmental Engineering, National Institute of Technology, Sendai College, 48 Nodayama, Medeshima-Shiote, Natori 981-1239, Japan.
† Author to whom correspondence should be addressed. Institute for Materials Research, Tohoku University, Sendai 980-8577, Japan; Tel.: +81 22 215 2118; Fax: +81 22 215 2116; E-mail: k_yamanaka@imr.tohoku.ac.jp

This journal is © The Royal Society of Chemistry 20xx

J. Mater. Chem. B, 2015, **00**, 1-3 | **1**

based (mass%) alloys for dental applications.[12–15] We subsequently investigated the high-temperature oxidation behaviour of Co–28Cr–9W–(0, 1, 2)Si alloys subjected to a heat treatment at 1273 K in air.[16] The addition of Si was shown to stabilise the dense Cr_2O_3 phase rather than cobalt oxides and to prevent oxidation by promoting Si segregation and the formation of a SiO_2 layer at the interface between the oxide film and the metal substrate. The thickness as well as the surface roughness of the surface oxide films was found to decrease between 0 and 1 mass% Si in the alloy but to remain approximately constant upon increasing the Si content to 2 mass%.

A number of alloying elements have been investigated as a means to improve the oxidation resistance of these alloys at elevated temperatures. Klein et al. investigated the effects of boron doping on the oxidation behaviour at 800–1000 °C of γ'-strengthened Co–Al–W–based alloys and found that the accumulation of boron in the inner oxide layer of high-boron-content alloys considerably improves their oxidation resistance by improving the adhesion of the oxide layer.[17,18] Their investigation of Cr-containing alloys revealed that in appropriate amounts, Cr significantly improves the oxidation resistance of the material through the formation of a protective Cr_2O_3 layer.[17] To the best of our knowledge, however, the effects of B on the properties of the oxide films formed on the surface of biomedical Co–Cr-based alloys with high (typically 28 mass%) Cr contents have not yet been elucidated. Therefore, the aim of the present study is to investigate the effects of the boron concentration on the morphology, crystal structure, and chemical composition of the oxide films formed on the surface of Co–Cr–W-based dental alloys. The oxidation behaviour of the alloys is also discussed. Since previous studies of the high-temperature oxidation behaviour of Co–Cr alloys have focused on relatively lengthy treatments (e.g. 1–100 h) at high temperatures,[17–21] this investigation of the initial stages (the first 15 min) of high-temperature oxidation will improve our understanding of the oxidation mechanisms in boron-containing Co-based alloys. The corrosion resistances of the prepared alloys were evaluated by performing potentiodynamic polarisation tests in a 0.9% NaCl solution to preliminarily determine the effect of boron addition on the uniform corrosion behavior of the prepared alloys.

Materials and methods

Sample preparation

Ni-free Co–28Cr–9W–1Si (mass%) alloys with boron concentrations of 0, 0.012, and 0.8 mass% were prepared by high-frequency vacuum induction melting. Hereafter, these alloys are referred to as 0B, 0.01B, and 0.8B, respectively. The Si content of the alloys was set to 1 mass% to maintain the same condition as our previous study.[16] Ingots which are 30 mm in diameter and weigh ~1 kg were subjected to hot forging, followed by a heat treatment at 1100 °C for 30 min. To perform the oxidation tests in air, the heat-treated materials

were cut into small plates (~10 × 10 mm^2 in cross section and 1 mm thick) using an electric discharge machine. In order to precisely characterise the oxide films, the specimens were ground with emery paper, polished with a 1-μm alumina suspension, and then finished with a 0.04-μm colloidal silica suspension. Finally, the samples were cleaned in ethanol using an ultrasonic cleaner and dried with a blower.

The oxidation heat treatment of the samples was performed in air at 1273 K for 15 min, which are the same conditions used in our previous study[16] and in practice, for preoxidation[8] and for sintering the dental porcelain. After the heat treatment, the samples were left to cool in air.

Characterisation of the oxide films

The initial microstructure of the samples, i.e. their microstructure prior to the oxidation treatment, was observed by scanning electron microscopy (SEM, Hitachi S-3400N, operating voltage: 15 kV). Electron backscatter diffraction (EBSD) analyses were also performed using a field-emission SEM (FESEM, FEI XL30S-FEG) system operated at 20 kV. The EBSD data were collected and analysed using an orientation image microscopy (OIM) system (TexSEM Laboratories, Inc.).

The surfaces of the oxide films were observed with a stereomicroscope (Leica M165 C, Leica Microsystems). An FESEM system (ULTRA 55, Carl Zeiss) operated at 15 kV was also employed to characterise the morphology of the oxides.

The crystalline structures of the oxide films formed on the surfaces of the Co–28Cr–9W–1Si alloys with different boron concentrations were characterised by grazing incidence X-ray diffraction (XRD, Rigaku Rotaflex RU-200B) with Cu Kα radiation. The incidence angle was set to 2°. The diffraction patterns were recorded for 2ϑ values ranging from 20° to 70°.

In order to determine the chemical state, composition, and depth profile of the oxide films, X-ray photoelectron spectroscopy (XPS, Axis Ultra DLD, Kratos) measurements were performed using monochromated Al Kα X-rays with an energy of 1486.7 eV. The XPS analysis area was 300 × 700 μm^2. Step sizes of 1 eV and 0.1 eV were used for the survey and precision scans, respectively. The depth profiles for the different elements of the oxide films were acquired by XPS after etching away the surface layers of the oxide films using an inert Ar gas ion gun (accelerating voltage: 4 kV). The etching and spectrum acquisition processes were alternately carried out to obtain the chemical depth profiles. SiO_2 was used as the etch-rate reference material to convert the etching time into a depth.

Potentiodynamic polarisation tests

The samples (15 mm in diameter) for the polarisation tests were cut from the heat-treated ingots and were mirror-polished with colloidal silica. The samples were kept in air for more than 1 day to stabilise the surface oxide films. Then, the mirror-polished disks were fixed to an electrode holder with a measurement area of 10 mm in diameter. The measurements were performed in a saline solution (0.9% NaCl solution). The effect of the dissolved oxygen was eliminated by bubbling nitrogen gas for at least 1.8 ks before measurement. The temperature of the saline solution was set to 310 K. A platinum plate and Ag/AgCl electrode were used as the

2 | J. Mater. Chem. B, 2012, 00, 1-3

This journal is © The Royal Society of Chemistry 20xx

counter and reference electrodes, respectively. The specimens were immersed in the solution for 3.6 ks to stabilise the potential of the specimens. The specimens were anodically polarised from −0.5 V to 1.5 V at a scanning rate of 1 mV s$^{−1}$.

Results

Initial microstructures

Figure 1 shows inverse pole figure maps (Figures 1a–c), phase maps (constructed from the EBSD scan data, Figures 1d–f), and SEM backscattered electron (BSE) images (Figures 1g–i) obtained for the alloy samples before the oxidation treatment. All alloys have a similar microstructure, consisting exclusively of the γ phase with a high density of annealing twins (Figures 1d–f). Precipitates, which appear as bright particles in the BSE images, are observed in all alloys. For the 0B and 0.01B specimens, these must be the σ phase.[14] In contrast, a cell-like domain microstructure is observed for the 0.8B alloy, in which fine recrystallised γ grains are surrounded by interdendritic constituents, which are probably the boride phase according to thermodynamic calculations. This must stem from the dendritic microstructure formed during casting and be retained during hot forging and the subsequent heat treatment. Accordingly, the addition of boron reduces the size of the γ grains. This effect is also evidenced for the 0.01B specimen, indicating that the boron atoms are dissolved at the grain boundaries[17] and hinder grain growth.

Appearance of surfaces after oxidation

Figure 2 shows optical micrographs of the surfaces of Co–28Cr–9W–1Si specimens with different boron contents. The oxidised surfaces change in colour from dark to metallic green as the boron concentration therein increases. This suggests that the properties (chemical state, thickness, etc.) of the surface oxide layer vary with the boron concentration in the alloy.

Figurers 3a–c show low-magnification secondary-electron SEM images of 0B, 0.01B, and 0.8B specimens, with the corresponding high-magnification images shown in Figures 3d–f. The oxide films have a nanocrystalline structure with facet-like particles ranging in size from tens to hundreds of nanometres. Although the grain structures of the surface oxide films are mostly homogeneous (this may be due in part to the addition of Si[16]), some variations are observed as a function of the boron concentration. Indeed, the grain structure of the 0B alloy (Figure 3d) is coarser than those of the 0.01B and 0.8B specimens (Figures 3e and 3f, respectively), with no significant difference between the latter two.

XRD analysis

Figure 4 shows the XRD patterns obtained from the alloy specimens after the oxidation heat treatment for 15 min at 1273 K. In agreement with our previous report,[16] these data show that the samples are not amorphous. The crystal structures of the oxide films depend on the B content of the alloys. Three oxides are identified, namely Cr_2O_3 (corundum-like structure, space group R-3c, Cr^{3+}), $CoCr_2O_4$ (spinel-like structure, Fd-3m, Co^{2+}/Cr^{3+}), and Co_3O_4 (spinel-like structure,

Fd-3m, Co^{2+}/Co^{3+}), with the 0B alloy containing all three. Owing to the addition of 1 mass% Si, the CoO phase (rock-salt-like structure, $C12/m1$, Co^{2+}) is not clearly detected in these XRD patterns.[16] The decrease in the intensities of the corresponding diffraction peaks shows that the cobalt oxide concentration decreases with the addition of boron to the alloys, such that the oxide films on the surfaces of the 0.01B and 0.8B specimens consist primarily of Cr_2O_3 and $CoCr_2O_4$.

XPS analysis

Surfaces. Figure 5 shows the results of XPS survey scans of the outermost layers of the Co–28Cr–9W–1Si–B samples subjected to an oxidation heat treatment at 1273 K for 15 min. The major peaks for various metallic elements, namely the Co $2p$, Cr $2p$, and W $4f$ peaks, and a high-intensity O $1s$ peak are all observed. A C $1s$ peak is also visible, but no signal assignable to boron appears in these survey spectra.

High-resolution XPS spectra obtained in the Co $2p$, Cr $2p$, W $4f$, and O $1s$ regions are presented in Figure 6. Within the depth probed with this technique, the metallic elements mostly exist as oxides, with no peak assignable to the elements in their metallic state (Figures 6a–c). (For consistency with the textbook,[22] the chemical states of the metallic elements in each specimen were determined from the positions of the corresponding peaks.) Figure 6a shows that Co is present in the form of Co^{2+} (Figure 6a), whereas the Cr $2p$ peaks in Figure 6b highlight the presence of both Cr^{3+} and Cr^{4+}, and the tungsten spectrum in Figure 6c is characteristic of W^{6+}. The remaining peaks in Figure 6b, which were also observed in our previous study[16] and cannot be assigned to Cr^{3+}/Cr^{4+}, are tentatively assigned to a CrOOH phase.[23] The O $1s$ peaks can be deconvoluted into at least three components, namely $O^{2−}$, hydroxide or hydroxyl groups (OH$^−$), and hydrates and/or absorbed water (H_2O).

The chemical compositions of the outermost oxide layers of the specimens were determined as summarised in Table 1. The carbon fraction, which originates from adventitious contamination and is not directly related to the investigated oxidation process, was excluded from the calculations. Likewise, N is considered a contaminant. There is no clear relationship between the surface concentrations of W and Si and the bulk boron concentration. Similarly, no clear trend emerges as a function of the boron content for the concentrations of CoO and Co(OH)$_2$ in these alloys, although the Co(OH)$_2$ content is always higher. This may be due to CoO reacting with absorbed water and forming Co(OH)$_2$ (CoO + H$_2$O → Co(OH)$_2$). In contrast, the Cr^{3+} and Cr^{4+} concentrations in the alloys increase with their boron content. This means that Cr oxidation is promoted by adding boron.

Depth profiles. The elemental depth profiles of the oxide films were obtained by XPS, as shown in Figure 7. The oxygen concentration is initially high at 45 at% and increases slightly to 55 at% in the subsurface region, where the fraction of Cr^{3+} also increases. The concentration of W-containing oxides is very low at all depths in these oxide films. The increase in the Si concentration immediately below the surface of the oxide film is more clearly visible for the 0B alloy than for the others. This might be due to the inhomogeneous

This journal is © The Royal Society of Chemistry 20xx

J. Mater. Chem. B, 2013, **00**, 1-3 | **3**

distribution of Si-rich layers in the initial stages of oxidation (here, within 15 min). Interestingly, the boron concentration is higher in the inner parts of the oxide films (Figures 7b and c). The formation of a B_2O_3 layer through the oxidation of some of the boron atoms is particularly evident at a depth of 100–600 nm for the higher boron content alloy (0.8B), as shown in Figure 7c.

The B $1s$ spectra obtained at different depths in the 0.8B specimen are shown in Figure 8. Peaks at a binding energy of ~193 eV are visible in the data obtained at depths of 80–840 nm. Additional peaks appear at ~188 eV at depths beyond 200 nm. The former are assigned to B_2O_3, whereas the latter most probably arise from boron atoms dissolved in the metal matrix. These results indicate that boron is segregated in the inner portions of these surface oxide films and reacts with oxygen, which penetrates from the surface during the oxidation heat treatment.

Thickness of the surface oxide films

The thickness of the oxide films was determined on the basis of the concentration depth profile of metallic Co (Table 2). The thicknesses of the surface oxide films remarkably decrease from 480 nm for the 0B alloy to ~300 nm for the 0.01B and 0.8B alloys. This means that the addition of boron in very small concentrations retards the high-temperature oxidation of these Co−Cr−W-based alloys.

Corrosion behaviour

Figure 9 shows the anodic polarisation curves obtained for the 0B and 0.01B alloys in a 0.9% NaCl solution at 310 K. All specimens were spontaneously passivated by anodic polarisation. The corrosion current (i_{corr}) and corrosion potential (E_{corr}), which were obtained by the Tafel fitting procedure, are presented in Table 3. The corrosion current density was almost the same for both alloys, although the corrosion potential of the 0B alloy was slightly lower than that of the 0.01B alloy. Further, boron doping did not markedly influence the passive current density. These results indicate that there were no degradation in the corrosion resistance and a significant change in surface characteristics owing to the addition of a small amount of boron.

Discussion

This study is devoted to understanding the effects of different boron concentrations on the oxide films formed on the surfaces of Co−Cr−W−Si-based dental alloys exposed to high temperatures. It should be noted that the 0B alloy in the present study has the same chemical composition (Co−28Cr−9W−1Si) as the 1Si alloy previously investigated.[16] The properties (surface chemistry, oxide film thicknesses, etc.) of these alloys are also similar. The XRD analysis conducted here reveals that as an oxide, cobalt is mainly present as Co_3O_4 on the 0B alloy, whereas the XPS data for the outermost surface reveal only CoO and $Co(OH)_2$, where the latter is possibly produced by reactions between the CoO phase and absorbed water. This means that CoO preferentially forms on the surface and that the Co_3O_4 concentration increases with the depth from the surface. This agrees well our previous

conclusion[16] that surface CoO transforms into Co_3O_4 during a high-temperature treatment. Cr was found to exist primarily as Cr_2O_3 (Cr^{3+}), with the presence of Cr^{4+} also evidenced, which may exist as CrO_2 (rutile-like structure, $P4/mnm$).[16] The W concentrations in all of the oxide films are very low (~1%), indicating that its role in the high-temperature oxidation process is less significant than that of the other metallic elements. Therefore, the present results should also be valid for other Co−Cr-based biomedical alloys such as Co−Cr−Mo alloys.

The high-temperature oxidation behaviour of Co−Cr-based alloys has been extensively studied for their use as heat-resistant superalloys.[19–21,24] Kofstad and Hed investigated the oxidation behaviour of Co−10 mass% Cr alloys at 1073–1573 K and observed double-layered oxide films with an outer CoO layer and an inner layer consisting of a mixture of CoO, Cr_2O_3, and $CoCr_2O_4$.[19,20] An increase in the Cr concentration was found to promote the formation of a single layer of Cr_2O_3;[21] this is also true for B-doped Co−Al−W-based γ/γ' superalloys.[17] Spinel-like $CoCr_2O_4$ may form via reactions between CoO and Cr_2O_3.[24] It has also been reported that CoO is gradually replaced by Cr_2O_3 under prolonged oxidation, forming a single-layered oxide film mostly consisting of Cr_2O_3.[25] The oxidation conditions used in this study (1273 K for 15 min) reveal the pre-equilibrium state of the oxide layers.

In a previous study, we showed how the addition of Si affects the high-temperature oxidation behaviour of Co−28Cr−9W-based dental alloys.[16] The formation of cobalt oxide was found to be retarded in the Si-containing alloys. This study also revealed that the addition of silicon accelerates the oxidation of Cr, leading to the formation of a Cr_2O_3 film. Elsewhere, Cr_2O_3 has been shown to have a protective effect on the alloy matrix, as it inhibits contact between the matrix and oxygen.[21] Since all of the alloys investigated in the present study contain Si, Cr_2O_3 is the main component of the oxide films formed thereon. Furthermore, boron is shown here to have a stabilising effect on the chromium-containing oxides, thereby significantly reducing the oxidation rate. A nanoscale layer enriched with B is clearly detected, in which the boron concentration is as high as ~10 at% in the 0.8B alloy (Figure 7c). A B_2O_3 phase is also identified in this alloy at the interface between the oxide film and the metal substrate, below which the boron concentration is higher than in the bulk of the alloy (Figure 7c). According to the Ellingham diagram, boron is more susceptible to oxidation than Cr. Boron—and also Si—should be preferentially oxidised, leading to the formation of nanoscale oxide layers. (The distribution of boron in these films is schematically illustrated in Figure 10.) The presence of a B_2O_3 layer is indeed confirmed here by XPS (Figure 8). These results suggest that a boron-enriched layer forms at the film/substrate interface and prevents oxygen diffusion from the surface during the very early stages of the oxidation heat treatment.

Delaying oxidation during manufacturing is desirable, as it reduces material loss and production cost, and improves the appearance and fitting of the resulting prostheses. This study shows that the co-addition of silicon and boron is an effective

4 | *J. Mater. Chem. B*, 2012, **00**, 1-3

This journal is © The Royal Society of Chemistry 20xx

means to improve the oxidation resistance of Co−Cr-based alloys, although the above-mentioned effect of boron doping should also be observed in Si-free Co−Cr-based alloys. Also of relevance is the chemical state of the oxide film, whose adhesion properties may be modified by the addition of boron. This is particularly important for PFM applications because the attachment of porcelain to the substrate relies on the formation of chemical bonds with the metallic oxides therein.[26] Further studies involving longer oxidation experiments are also required to clarify the kinetics of the high-temperature oxidation processes of these alloys and their subsequent suitability for PFM applications.

On the other hand, the addition of too much boron results in the precipitation of borides, as shown in Figure 1i. Although sufficient corrosion resistance can be maintained when only a small amount of boron (0.012 mass%) is alloyed, the boride might also be detrimental to the corrosion and mechanical properties (in particular, the ductility) of the alloys. In addition, an increase in the boron concentration from 0.012 to 0.8 mass% did not significantly alter the high-temperature oxidation resistance. The boron concentrations in these alloys should be tailored to the particular application envisaged from various aspects, e.g. the mechanical properties, the corrosion resistance, the surface characteristics, the bonding to porcelain, biocompatibility, etc.

Conclusions

In this study, we investigated the high-temperature oxidation behaviour of Ni-free Co−28Cr−9W−1Si alloys with different boron contents (0−0.8 mass%) during heat treatment in air at 1273 K for 15 min. The oxide films formed on the surfaces of the specimens were analysed using SEM, XRD, and XPS. The chemical compositions of these surface layers vary with the B concentration in the bulk, with the addition of boron stabilising the dense Cr_2O_3 phase in the oxide films. Accordingly, the films have a faceted morphology, with smaller facets observed at higher boron concentrations. Nanoscale boron segregation was observed at the interface between the oxide film and the metal substrate. The penetration of oxygen from the alloy surface leads to the formation of B_2O_3 in these boron-enriched regions. Since B_2O_3 and Cr_2O_3 prevent oxygen diffusion, the surface oxide films on the boron-containing alloys are thinner; however, no additional thinning was observed upon increasing the boron content from 0.01 to 0.8 mass%. The stabilisation of the dense Cr_2O_3 phase also contributes to the enhanced oxidation resistance of the boron-containing alloys at elevated temperatures. We also preliminarily revealed that a small amount of boron does not alter the corrosion resistance of the alloys. This phenomenon can be exploited to improve the performance of Co−Cr-based alloys for various applications.

Acknowledgements

Notes and references

1   E. D. Rekow, *J. Am. Dent. Assoc.*, 2008, **137**, 5–6.
2   F. Beuer, J. Schweiger, M. Eichberger, H. F. Kappert, W. Gernet and D. Edelhoff, *Dent. Mater.*, 2009, **25**, 121–128.
3   M. Özcan, *J. Oral Rehabil.*, 2003, **30**, 265–269.
4   S. Viennot, F. Dalard, G. Malquarti and B. Grosgogeat, *J. Prosthet. Dent.*, 2006, **96**, 100–103.
5   E. Denkhaus and K. Salnikow, *Crit. Rev. Oncol. Hematol.*, 2002, **42**, 35–56.
6   W. C. Wagner, K. Asgar, W. C. Bigelow and R. A. Flinn, *J. Biomed. Mater. Res.*, 1993, **27**, 531–537.
7   I. Murakami, J. Vaidyanathan, T. K. Vaidyanathan and A. Schulman, *Dent. Mater.*, 1990, **6**, 217–222.
8   B. Henriques, D. Soares and F. S. Silva, *Mater. Sci. Eng. C*, 2012, **32**, 2374–2380.
9   J. R. Mackert, E. E. Parry, D. T. Hashinger and C. W. Fairhurst, *J. Dent. Res.*, 1984, **63**, 1335–1340.
10 J. R. Mackert, E. E. Parry and C. W. Fairhurst, *Dent. Mater.*, 1985, **1**, 111–4.
11 Y. Wu, J. B. Moser, L. M. Jameson and W. F. Malone, *J. Prosthet. Dent.*, 1991, **66**, 439–444.
12 K. Yamanaka, M. Mori, K. Kuramoto and A. Chiba, *Mater. Des.*, 2014, **55**, 987–998.
13 K. Yamanaka, M. Mori and A. Chiba, *Mater. Lett.*, 2014, **116**, 82–85.
14 K. Yamanaka, M. Mori and A. Chiba, *Mater. Sci. Eng. A*, 2014, **592**, 173–181.
15 K. Yamanaka, M. Mori and A. Chiba, *Mater. Des.*, 2014, **57**, 421–425.
16 K. Yamanaka, M. Mori and A. Chiba, *Corros. Sci.*, 2015, **94**, 411–419.
17 L. Klein, Y. Shen, M. S. Killian and S. Virtanen, *Corros. Sci.*, 2011, **53**, 2713–2720.
18 L. Klein, B. von Bartenwerffer, M. S. Killian, P. Schmuki and S. Virtanen, *Corros. Sci.*, 2014, **79**, 29–33.
19 P. Kofstad and A. Hed, *J. Electrochem. Soc.*, 1969, **116**, 224–229.
20 P. K. Kofstad and A. Z. Hed, *J. Electrochem. Soc.*, 1969, **116**, 229–234.
21 P. K. Kofstad and A. Z. Hed, *J. Electrochem. Soc.*, 1969, **116**, 1542–1550.
22 J. F. Moulder, W. F. Stickle, P. E. Sobol and K. D. Bomben, *Handbook of X-ray Photoelectron Spectroscopy*, Physical Electronics, Eden Prairie, 2nd edn., 1995.
23 Y. Shibasaki, F. Kanamaru and M. Koizumi, *Mater. Res. Bull.*, 1970, **5**, 1051–1058.

This journal is © The Royal Society of Chemistry 20xx

J. Mater. Chem. B, 2013, **00**, 1-3 | **5**

Journal of Materials Chemistry B Accepted Manuscript

24 D. L. Douglass and J. S. Armijo, *Oxid. Met.*, 1971, **3**, 185–202.
25 Y. Li, N. Tang, P. Tunthawiroon, Y. Koizumi and A. Chiba, *Corros. Sci.*, 2013, **73**, 72–79.
26 T. Johnson, R. Van Noort and C. W. Stokes, *Dent. Mater.*, 2006, **22**, 330–337.

Figure and table captions

Figure 1. (a–c) Inverse pole figure maps, (d–f) phase maps, and (g–i) scanning backscattered electron (BSE) micrographs of Co–28Cr–9W–1Si–B alloys containing (a, d, g) 0, (b, e, h) 0.01, and (c, f, i) 0.8 mass% boron before the oxidation treatment. The black, white, and red lines in the boundary maps indicate high-angle boundaries with misorientation angles larger than 15°, low-angle boundaries with misorientation angles of 2–15°, and annealing-twin boundaries with a Σ3 coincidence site-lattice relationship, respectively. Image quality maps are overlaid on the corresponding phase maps.

Figure 2. Optical micrographs of Co–28Cr–9W–1Si–B alloys containing (a) 0, (b) 0.01, and (c) 0.8 mass% boron following a heat treatment in air at 1273 K for 15 min.

Figure 3. Scanning (secondary) electron micrographs of Co–28Cr–9W–1Si–B alloys containing (a, d) 0, (b, e) 0.01, and (c, f) 0.8 mass% boron following a heat treatment in air at 1273 K for 15 min.

Figure 4. X-ray diffractograms of Co–28Cr–9W–1Si–B (mass%) alloys with different boron contents.

Figure 5. X-ray photoelectron spectroscopy survey scans of Co–28Cr–9W–1Si–B (mass%) alloys with different boron contents.

Figure 6. X-ray photoelectron spectra and peak deconvolution in the (a) Co *2p*, (b) Cr *2p*, (c) W *4f*, and (d) O *1s* regions obtained for Co–28Cr–9W–1Si–B (mass%) alloys containing boron in different concentrations.

Figure 7. Elemental depth profiles in Co–28Cr–9W–1Si–B alloys containing (a) 0, (b) 0.01, and (c) 0.8 mass% boron, as determined by X-ray photoelectron spectroscopy.

Figure 8. X-ray photoelectron spectra in the B *1s* region obtained at different depths in Co–28Cr–9W–1Si–B alloys containing 0.8 mass% boron.

Figure 9. Potentiodynamic polarisation curves for the 0B and 0.01B alloys in a 0.9% NaCl solution at 310 K.

Figure 10. Schematic of the boron distribution in the oxide film formed on boron-doped Co–28Cr–9W–1Si (mass%) alloys.

Table 1. Surface chemical composition (at%) of Co–28Cr–9W–1Si–B (mass%) alloys, as determined by X-ray photoelectron spectroscopy.

Table 2. Thicknesses, as determined from X-ray photoelectron spectroscopy depth profiles, of the oxide films formed on Co–28Cr–9W–1Si–B (mass%) alloys with different boron contents.

Table 3. Corrosion current (i_{corr}) and corrosion potential (E_{corr}) for the 0B and 0.01B alloys, as determined by the Tafel extrapolation fitting.

6 | *J. Mater. Chem. B*, 2012, **00**, 1-3

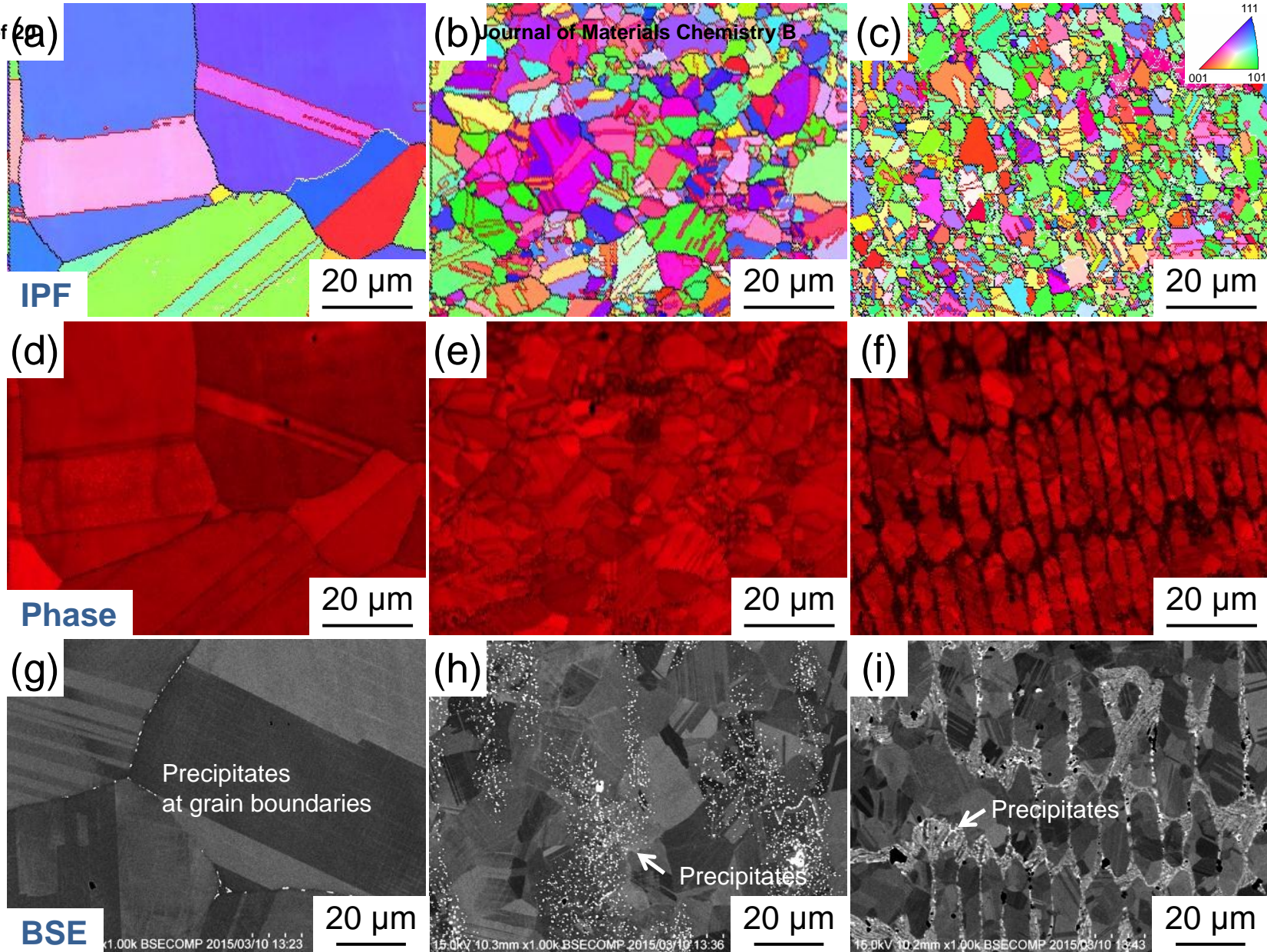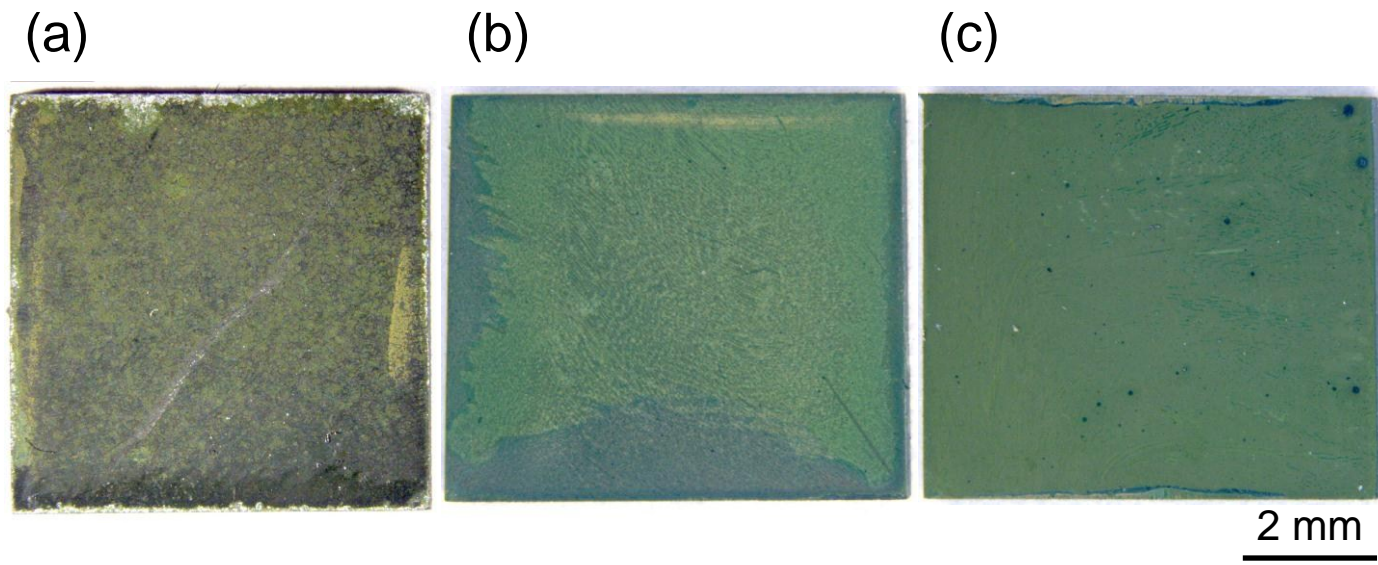This journal is © The Royal Society of Chemistry 20xx

Figure 1. (a−c) Inverse pole figure maps, (d−f) phase maps, and (g−i) scanning (backscatter) electron (BSE) micrographs of Co–28Cr–9W–1Si–B alloys containing (a, d, g) 0, (b, e, h) 0.01, and (c, f, i) 0.8 (mass%) boron before oxidation treatment. The black, white, and red lines in the boundary maps indicate high-angle boundaries with misorientation angles larger than 15°, low-angle boundaries with misorientation angles of 2–15°, and annealing-twin boundaries with a Σ3 coincidence site-lattice relationship, respectively. In the phase maps, the corresponding image quality maps are overlapped.

Figure 2. Optical micrographs of Co–28Cr–9W–1Si–B alloys containing (a) 0, (b) 0.01, and (c) 0.8 (mass%) boron following heat treatment in air at 1273 K for 15 min.
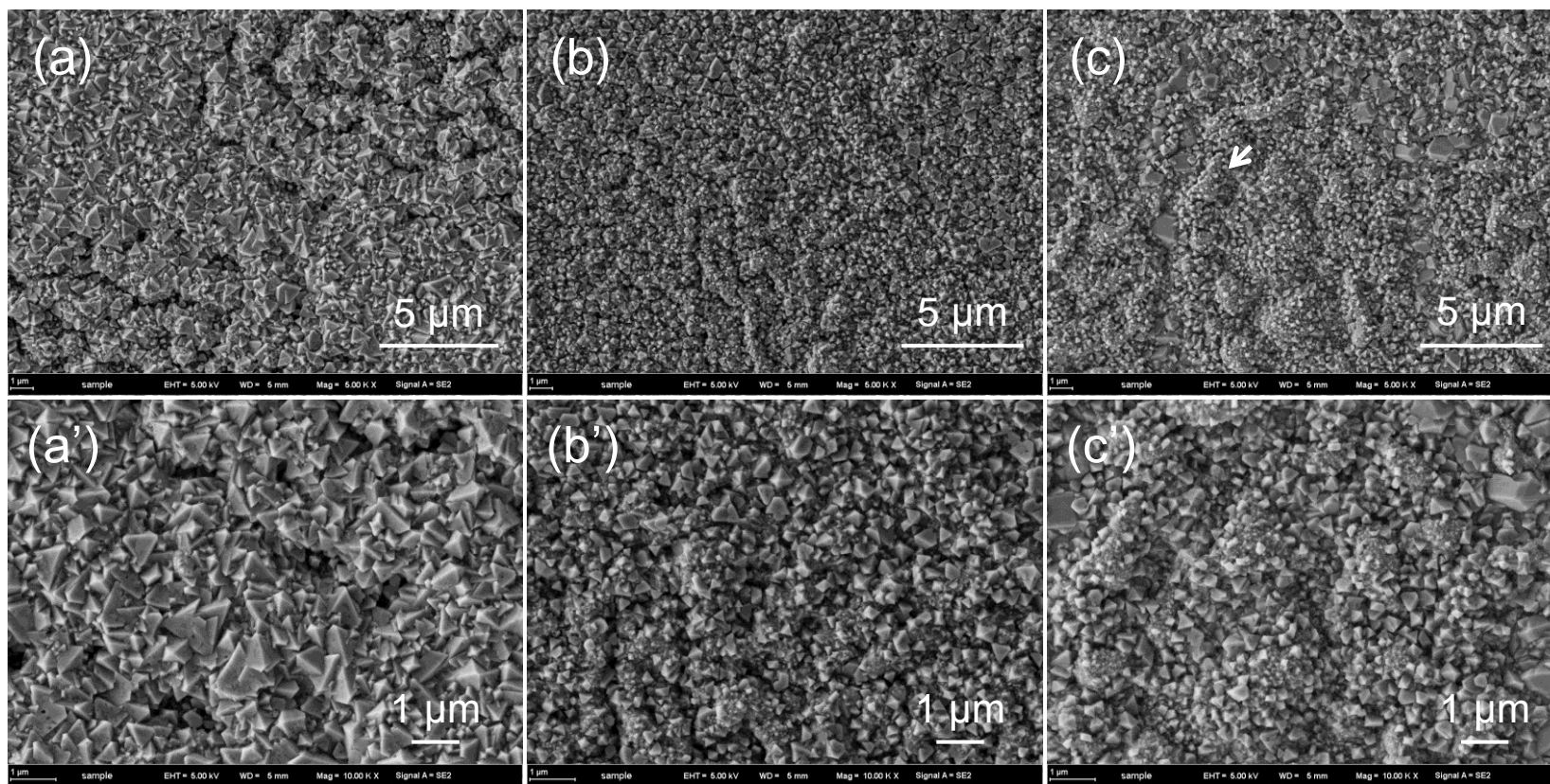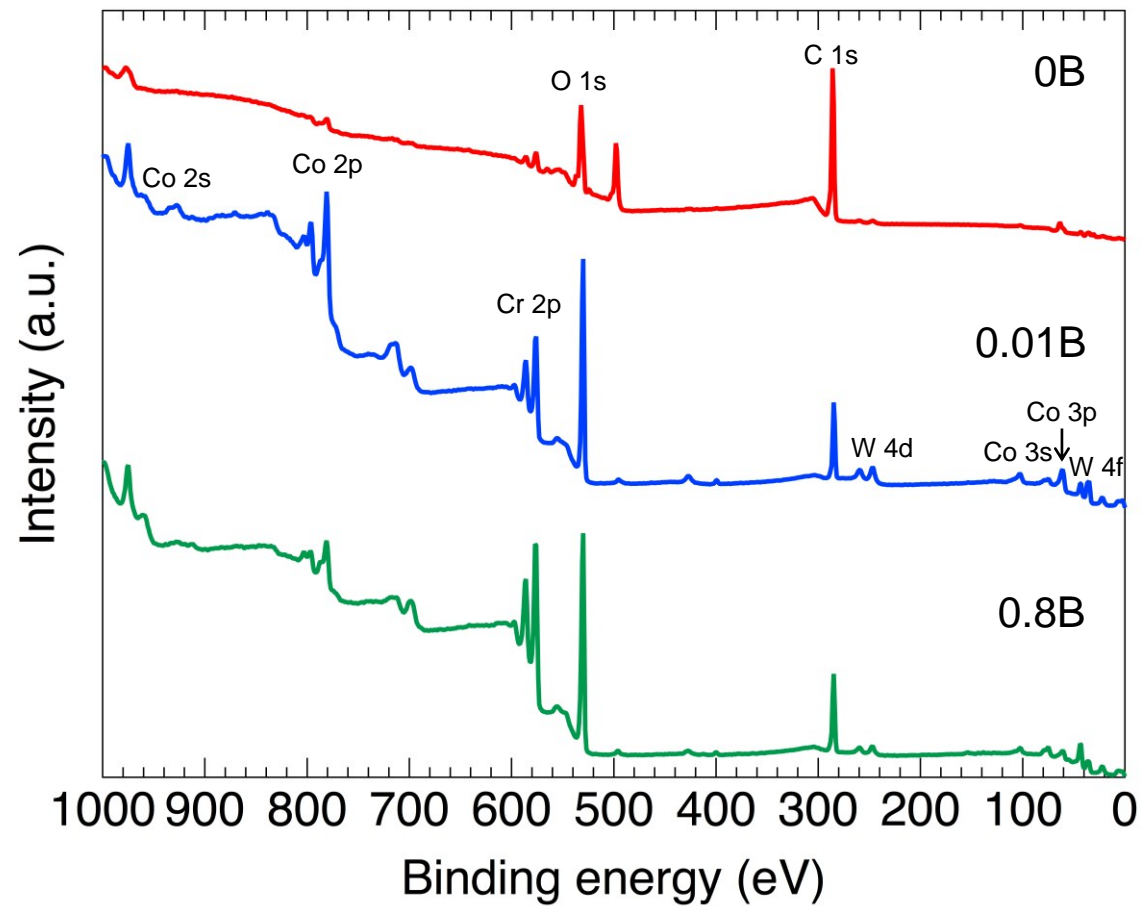
Figure 3. Scanning (secondary) electron micrographs of Co–28Cr–9W–1Si–B alloys containing (a, d) 0, (b, e) 0.01, and (c, f) 0.8 (mass%) boron following heat treatment in air at 1273 K for 15 min.

Figure 4. X-ray diffractograms of Co−28Cr−9W−1Si–B (mass%) alloys with different boron contents.

Figure 5. X-ray photoelectron spectroscopy survey scans of Co−28Cr−9W−1Si−B (mass%) alloys with different boron contents.
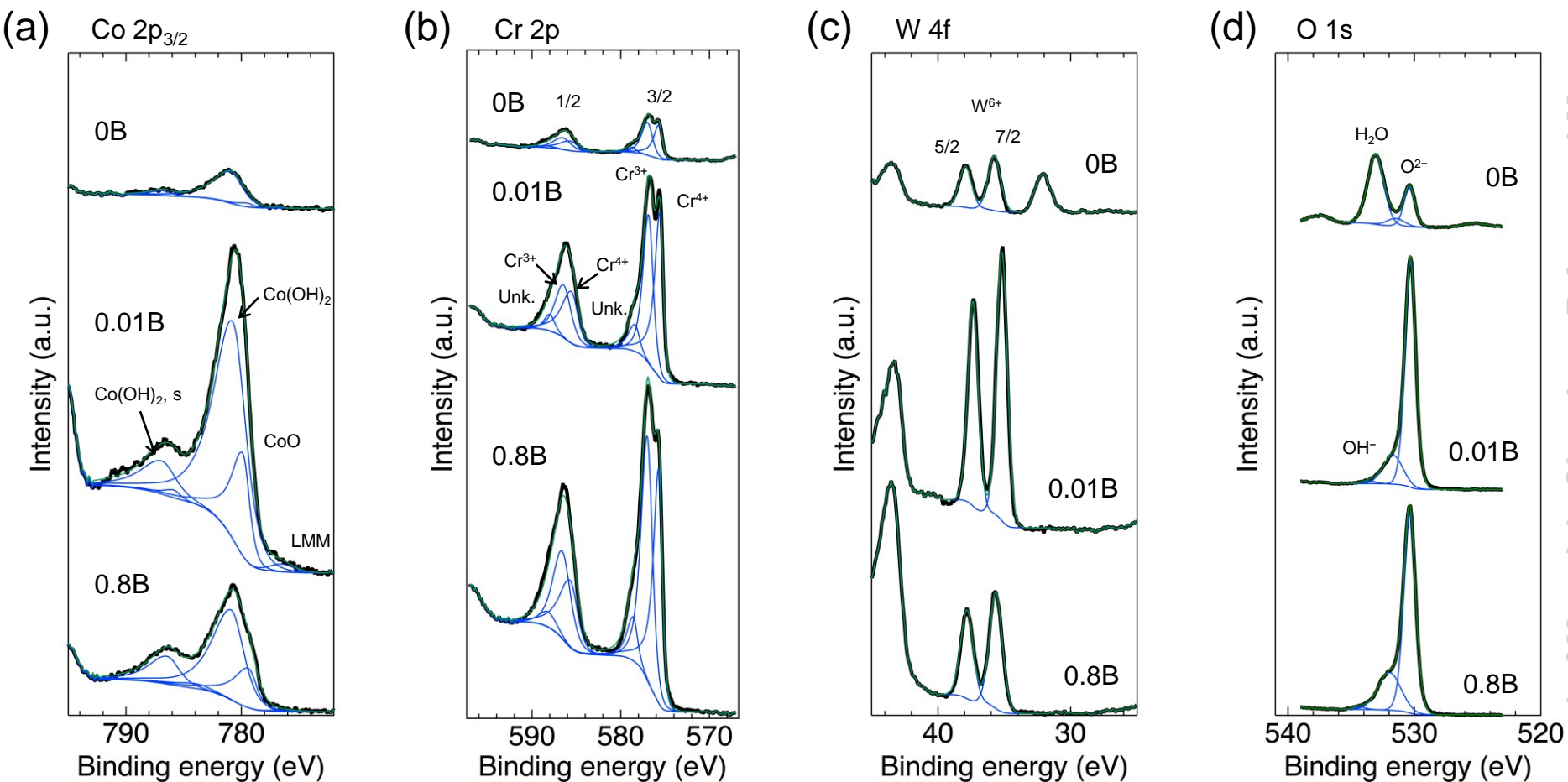
Figure 6. X-ray photoelectron spectra and peak deconvolution in the (a) Co *2p*, (b) Cr *2p*, (c) W *4f*, and (d) O *1s* regions obtained for Co−28Cr−9W−1Si−B (mass%) alloys containing boron in different concentrations.
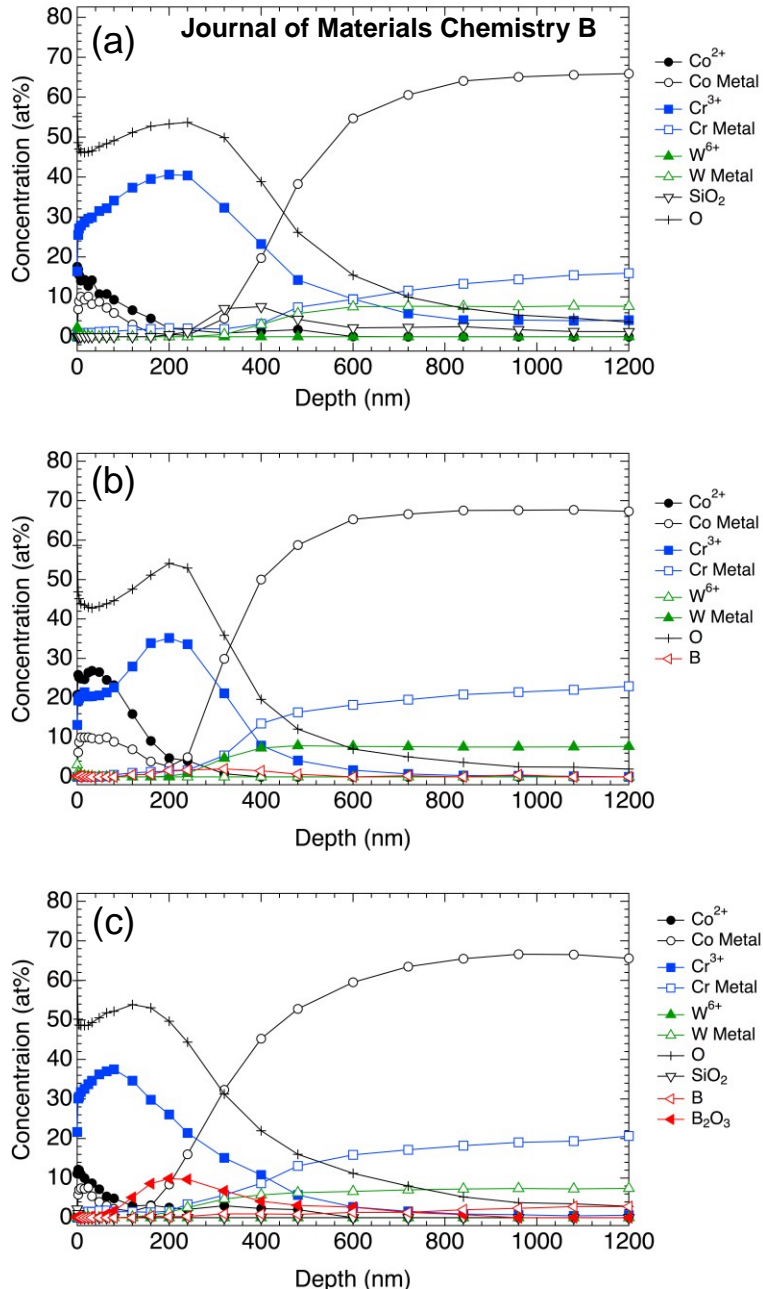
Figure 7. Elemental depth profiles in Co−28Cr−9W−1Si−B alloys containing (a) 0, (b) 0.01, and (c) 0.8 (mass%) boron, as determined by X-ray photoelectron spectroscopy.
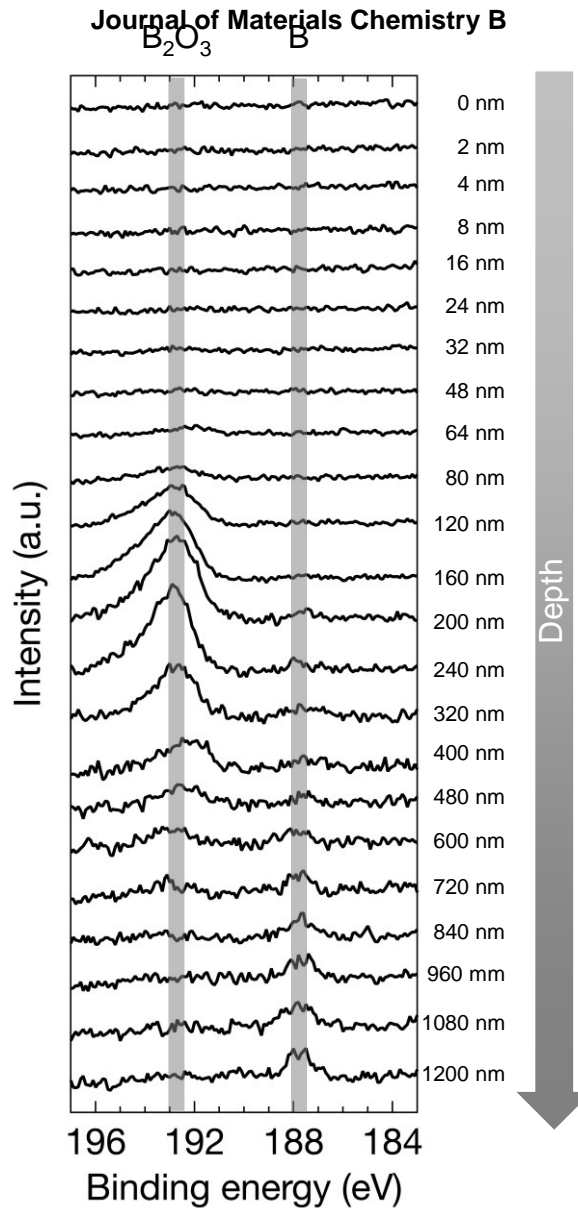
Figure 8. X-ray photoelectron spectra in the B *1s* region obtained at different depths in Co−28Cr−9W−1Si−B alloys containing 0.8 (mass%) boron.
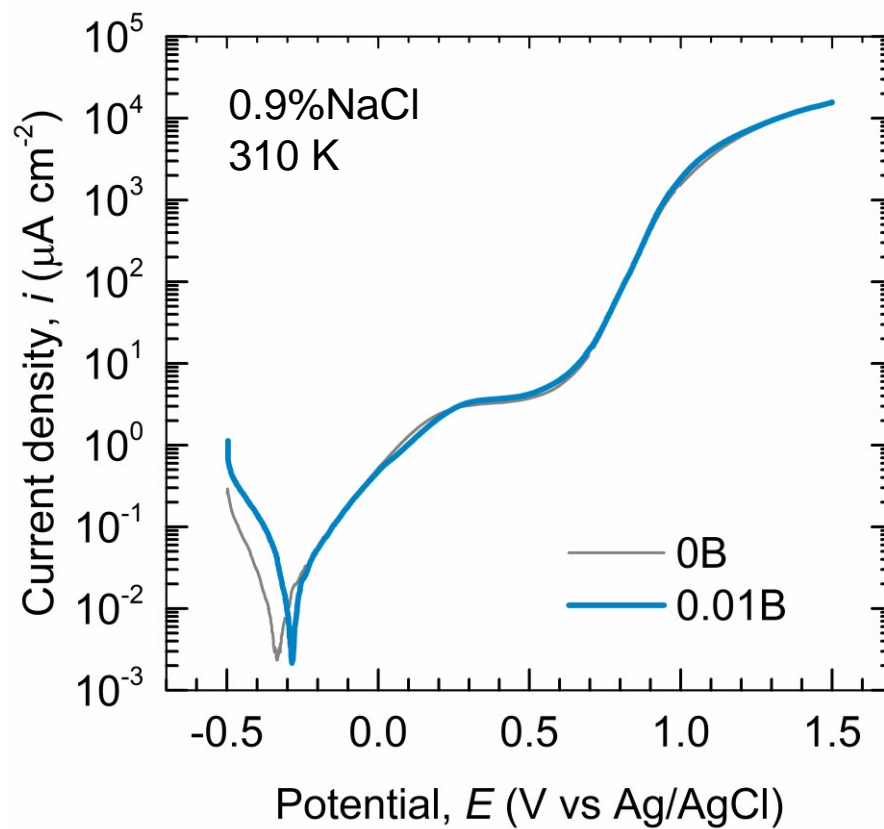
Figure 9. Potentiodynamic polarization curves for the 0B and 0.01B alloys in 0.9% NaCl solution at 310 K.
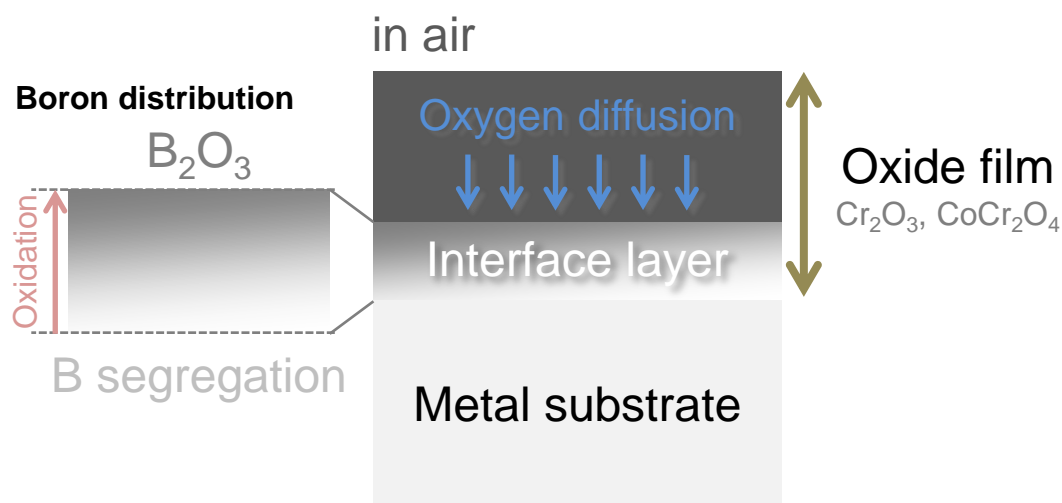
Figure 10. Schematic illustration of the boron distribution in the oxide film formed on boron-doped Co−28Cr−9W−1Si (mass%) alloys.

Table 1. Surface chemical composition (at%) of Co−28Cr−9W−1Si−B (mass%) alloys, as determined by X-ray photoelectron spectroscopy.

	0B	0.01B	0.8B
CoO	0.28	3.74	1.88
$Co(OH)_2$	4.47	14.09	6.12
Cr^{3+}	4.26	7.26	12.68
Cr^{4+}	3.89	7.68	10.72
Cr unknown	0.52	1.50	2.19
W^{6+}	1.26	2.16	1.06
O^{2-}	21.54	49.05	45.30
OH^-	6.46	11.21	16.27
H_2O	55.65	0.74	0.59
N	1.10	0.18	0.39
Si	0.72	0.58	1.06

Table 2. Thicknesses, as determined from X-ray photoelectron spectroscopy depth profiles, of the oxide films formed on Co−28Cr−9W−1Si−B (mass%) alloys with different boron contents.

	Thickness of oxide scale (nm)
0B	480
0.01B	333
0.8B	293

Table 3. Corrosion current (i_{corr}) and corrosion potential (E_{corr}) for the 0B and 0.01B alloys, as determined by the Tafel extrapolation fitting.

Alloy	i_{corr} ($\mu A\ cm^{-2}$)	E_{corr} (V vs Ag/AgCl)
0B	0.015 ± 0.010	−0.32 ± 0.04
0.01B	0.014 ± 0.005	−0.28 ± 0.01

Graphical abstract